Journal of Materials Research and Technology 40 (2026) 991–1002

Contents lists available at ScienceDirect

Journal of Materials Research and Technology

journal homepage: www.elsevier.com/locate/jmrt

Powder-bed Fusion additive manufacturing of 316L stainless steel using short-wavelength diode point melting

S. Can Erman [a,*], Alkim Aydin [b,c], Kamran Mumtaz [a]

[a] School of Mechanical, Aerospace, and Civil Engineering, The University of Sheffield, Sheffield, S1 4TD, United Kingdom
[b] Department of Mechanical Engineering, Gazi University, Ankara, 06570, Türkiye
[c] Additive Manufacturing Technologies Research and Application Center - EKTAM, Gazi University, Ankara, 06560, Türkiye

ARTICLE INFO

Keywords:
Diode point melting (DPM)
Laser powder bed fusion (LPBF)
Stainless steel 316L (SS316L)
Microstructure control
450 nm diode lasers

ABSTRACT

Diode Point Melting (DPM) is an alternative additive manufacturing powder-bed melting approach that combines multiple low-power, short-wavelength lasers into a single spot that is raster-scanned by an XY gantry to selectively melt deposited powder. In this study, the DPM laser head is composed of eight 450 nm diodes (~35 W total) focused to ~100 × 150 μm and is used to fabricate 316L stainless steel. Parts achieve >98 % relative density while operating at slower scan speeds and estimated lower cooling rates than Laser Powder Bed Fusion (LPBF) ($\approx 6.66 \times 10^4$ K s^{-1} vs $\sim 10^7$ K s^{-1}). The DPM microstructure is distinguished by larger grains (~18 μm) and larger cellular sub-grains (~2 μm) relative to the typical LPBF of 316L. It was demonstrated that cellular size decreases with increasing scan speed, evidencing cooling-rate control of the sub-grain structure. Mechanical characterisation shows a modest reduction in elastic modulus and Vickers hardness compared with LPBF-processed 316L, attributed to grain coarsening and slightly higher porosity, while values remain above those of conventionally manufactured 316L. These findings demonstrate potential for DPM to be a low-cost and accessible alternative to LPBF with unique microstructural characteristics.

1. Introduction

Laser Powder Bed Fusion (LPBF) is a widely utilised additive manufacturing technique that serves as an alternative to conventional manufacturing methods. It enables the fabrication of fully dense, geometrically complex components by selectively melting metal powder layer by layer using a fiber laser. Although various metallic powders such as titanium alloys, nickel-based super alloys, and aluminium alloys are currently processed using LPBF, approximately one-third of all publications in the metal additive manufacturing literature focus on steels due to their wide range of industrial applications and superior mechanical properties [1]. Stainless steel 316L (SS316L), in particular, is a widely utilised feedstock material due to its broad range of applications, including nuclear plants [2,3], biomedical [4], and marine applications [5]. Its widespread adoption is attributed to its superior corrosion resistance [6,7], high strength [8], biocompatibility [7], and cost-effectiveness [9].

The mechanical properties of steel components fabricated through LPBF may differ significantly from those of conventionally manufactured parts, primarily due to the unique microstructure that arises from the rapid solidification inherent to the LPBF process. Tolosa et al. [10] reported that SS316L samples exhibit higher yield strength while maintaining significant elongation than their wrought counterparts. In addition to the enhanced yield strength, parts produced via LPBF exhibit higher tensile strength [11] and elastic modulus [12] than wrought parts. Therefore, microstructural characterisation in metal additive manufacturing is essential for controlling and tailoring the mechanical properties of fabricated components. Due to the layer-wise nature of fabrication in LPBF, grains tend to elongate along the building direction [13], resulting in a pronounced crystallographic texture characterised by a high fraction of <001> oriented grains [13,14]. Nevertheless, several studies have reported the presence of grains oriented along the <101> and <111> directions [15–18] to the building direction, attributed to the scanning strategy employed during fabrication [16,17]. At the sub-grain level, a cellular microstructure is commonly observed in SS316L due to the high cooling rates inherent in LPBF.

Researchers have particularly focused on the microstructural customisation of SS316L [14,19–21] in terms of cellular structure; the size of the cell size significantly influences the strength and ductility of the fabricated parts [8]. Bertoli et al. successfully validated the good

---

[*] Corresponding author.
E-mail address: scerman1@sheffield.ac.uk (S.C. Erman).

https://doi.org/10.1016/j.jmrt.2025.12.214
Received 29 August 2025; Received in revised form 2 December 2025; Accepted 20 December 2025

agreement between empirically estimated cooling rates and Rosenthal's analytical solutions, demonstrating that cellular structure size decreases with increasing cooling rate [20]. Some researchers have also confirmed a decreasing trend in cellular structure size with increasing scanning speed, which corresponds to a higher cooling rate [19,22]. Krahmalev et al. [23] investigated the effects of further annealing at 1050 °C and reported that the cellular structure disappears due to recrystallisation, leading to a decrease in hardness. Li et al. [24] demonstrated that heat treatment at 1200 °C leads to an increase in grain size and a reduction in residual stress, resulting from rapid solidification in as-built SS316L. Apart from the cellular structure works in the literature, Gao et al. [25] revealed that a lower hatch distance and the application of remelting result in a microstructure free of geometrically necessary dislocations, characterised by equiaxed grains. Liu et al. [26] reported that remelting significantly increases the grain size of the sample compared to the as-built LPBF condition, transforming the microstructure from a cellular to a columnar substructure. Navarre et al. [27] demonstrated that the addition of 2 wt% Al to SS316L transforms the microstructure from fully γ-austenite in the as-built state to fully δ-ferrite. There are a limited number of studies in the literature that investigate the effect of different process parameters within the same sample. Elkaseer et al. [28] employed two distinct regions on a single sample, each processed with different scanning speeds, hatch distances, and laser powers, to investigate their influence on the surface roughness and hardness of AISI 420 parts. Sofinowski et al. [29] demonstrated that rotating the scanning angle enables control of the crystallographic texture along the build direction.

Despite its advantages, LPBF-manufactured parts also encounter several challenges, such as micro-cracking [30], distortion [31], and residual stress [32], low laser absorptivity of metal powders [33], in addition to the high equipment and production costs [32] associated with the process. Ye et al. [34] report that the poor fatigue performance of LPBF-produced samples is associated with their surface roughness, porosity, microstructural characteristics, and residual stress state. A further challenge in LPBF lies in processing highly reflective materials, such as aluminium alloys [35] and pure copper [36], which exhibit low absorptivity at the wavelengths commonly employed in the technique. Literature on process parameter optimisation for SS316L in LPBF indicates that the required laser power typically ranges from 100 to 380 W [37–40]; however, higher power levels between 1000 and 2000 W have also been employed in the study to achieve optimal energy density conditions [41]. Processing materials with higher thermal conductivity requires increased energy input, which in turn leads to higher manufacturing costs due to the use of high-power lasers [42]. Stainless steels such as SS316L and 17-4 PH exhibit higher thermal conductivity compared to other commonly used metal powders like Inconel 718, Inconel 625, and Ti6Al4V [43]. Therefore, processing SS316L using low-power diode lasers presents both an interesting and challenging research question in the field of laser-based additive manufacturing.

This work presents Diode Point Melting (DPM), a low-power, low-cost alternative to traditional LPBF, coupling multiple low-power short-wavelength (450 nm) diode lasers into a single. The DPM laser head is mounted on a translating x-y gantry rail for selective SS316L laser processing across the powder bed. The laser absorptivity of SS316L powder increases by approximately 10 % when using 450 nm diode lasers compared to 1070 nm fiber lasers [44]. The capability of producing high-density parts, achieving up to 99.4 % relative density, was recently validated with Ti6Al4V [45] alongside investigations into the effect of in-situ dynamic laser area heating to enhance thermal control [46]. In this study, SS316L will be processed using DPM, this material presents new challenges due to its higher thermal conductivity and powder density compared to previous DPM-processed materials (Ti64). DPM SS316L component microstructural characterisation is performed (e.g. SEM, EBSD, XRD, EDS) as well as mechanical testing. Additionally, in this work, the scanning speed was varied on a layer-by-layer basis to tailor the microstructure along the build direction in DPM-processed SS316L, addressing the existing research gap on microstructural customisation.

2. Materials and methods

2.1. Material specifications

Spherical-shaped SS316L powder with size quantiles Dv (10) = 17.9 μm, Dv (50) = 28.5 μm, and Dv (90) = 43.9 μm is utilised in all experiments. Fig. 1(a) illustrates the particle size distribution of the powder as measured using the Malvern Mastersizer 3000. Fig. 1(b) confirms the spherical morphology of the powder, as observed under SEM at 500× magnification. The chemical composition of the powder is presented in Table 1. The austenitic stainless steels are broadly preferred in corrosive environments due to their excellent corrosion resistance [6], in addition to their superior mechanical properties and cost-effectiveness [47].

2.2. Experimental setup and procedure

In this study, eight individual 450 nm diode lasers, each with an optical output of approximately 4.4 W, are focused on a single spot (see Fig. 2(a)). An air-cooling system is integrated into the enclosure to prevent the diode laser temperature from exceeding its operational limits. Additionally, focusing and collimating lenses are used to direct

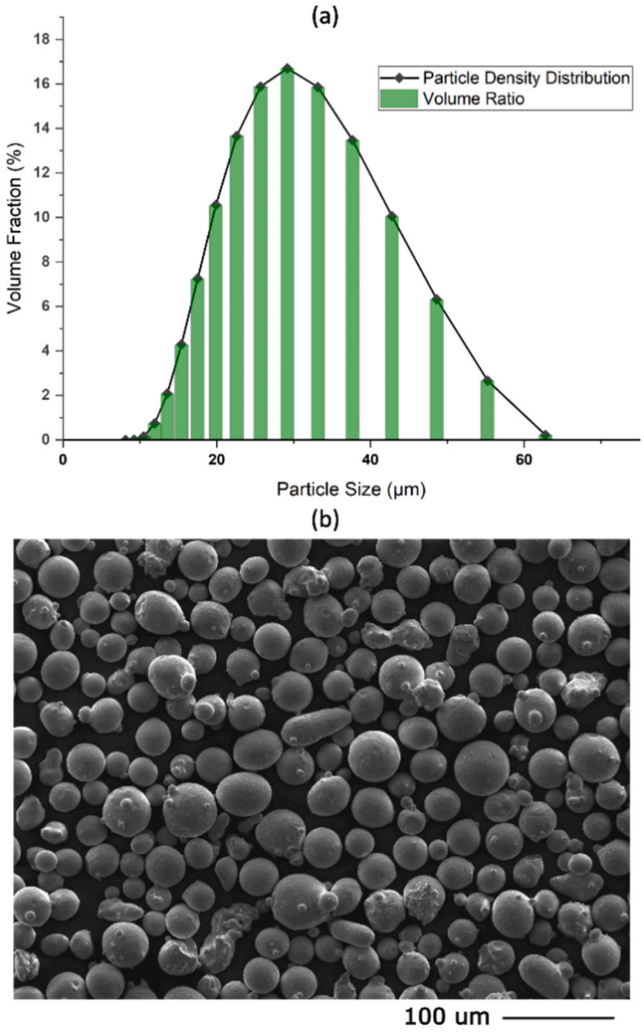

Fig. 1. (A) The particle size distribution of SS316L powder, (b) particle morphology of SS316L under SEM at 500x.

Table 1
The elemental composition of SS316L powder.

Element	Fe	Cr	Ni	Mo	C	Mn	Si	Others
Wt (%)	Balance	17.6	12.6	2.34	0.016	0.89	0.57	0.13

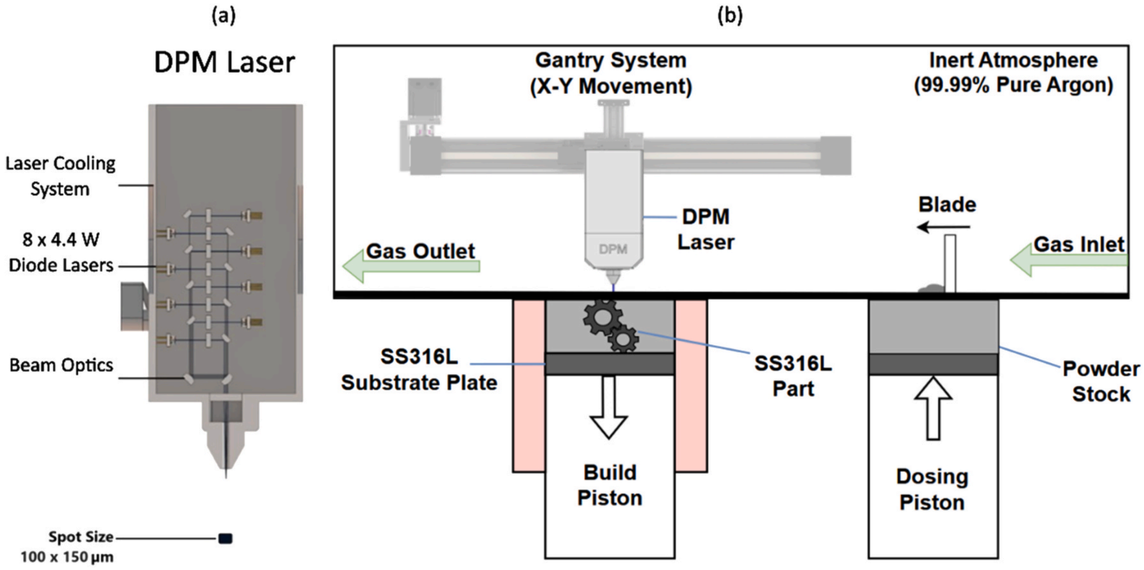

Fig. 2. (A) The schematics of the DPM laser, (b) the schematics of the experiment setup of DPM.

and focus the laser beams into a single spot. The resulting laser spot has a rectangular shape with dimensions of 100 × 150 μm^2 at focus. In contrast to the galvo scanning system used in industrial LPBF machines, the custom-built laser system, with a total optical power of 35 W, moves along the x-y direction using a gantry system to melt the powder (see Fig. 2(b)). It offers a solution to the scalability limitations associated with LPBF by enabling the fabrication of larger components [48]. Furthermore, 99.99 % pure shield argon is purged into the experiment setup before the processing and oxygen content is monitored during the experiment (kept under 1000 ppm).

In this paper, two hatch distances are employed in the fabrication of SS316L in DPM, as 75 µm and 100 µm correspond to 50 % and 33 % laser spot overlap (overlap is given from the long side of the laser spot). Additionally, the scanning speed parameters range from 750 to 1800 mm/min (12.5–30 mm/s). The scanning speed and hatch distance parameters are selected to be comparable to those used in a previous study conducted with DPM [45]. The layer thickness is set to 30 µm, consistent with literature studies on LPBF-processed SS316L [49–52]. The laser power is maintained at a maximum of 35 W, as previous research on DPM processing of Ti6Al4V has shown that using full power leads to improved densification compared to using half power [45].

In all experiments, a total of 50 layers with a thickness of 30 µm were processed following the initial 25 layers, which were excluded from all subsequent analyses. The top 50 layers are considered for all analyses. To eliminate any random effects during processing, at least three samples were produced for each parameter set, with fabrication carried out in different regions of the substrate. In brief, a full factorial experimental design is employed, incorporating two process parameters: hatch distance (two levels) and scanning speed (eight levels). This results in 16 parameter combinations, each replicated at least three times, yielding a minimum of 48 experimental runs. Laser power and layer thickness remain constant throughout. The design facilitates the analysis of both main and interaction effects, while replication enables estimation of experimental error and assessment of statistical significance.

Following the investigation of the as-built DPM samples, remelting is carried out using both full power (35 W) and half power (17.5 W) to examine its effect on relative density and melt pool formation. In this process, each layer of the sample is remelted using the same scanning strategy as in the initial pass.

Additionally, samples consisting of 80 layers are fabricated at scanning speeds of 1200, 1350, 1500, and 1800 mm/min, identified as the optimal scanning speeds for densification. A hatch distance of 100 µm is employed in this study, based on the densification results, which indicate it as the optimal value for achieving a higher relative density. These samples are then analysed to evaluate cellular structure size, to understand the influence of cooling rate on microstructural control.

2.3. *Material characterisation*

Samples are subjected to a metallography procedure after cutting. First, the samples are cross-sectioned and then subjected to automated grinding and polishing. P320 to P4000 waterproof grinding papers, followed by a Chemomet cloth with a 0.06 µm colloidal silica suspension, are used sequentially for grinding and polishing. Following the ultrasonic cleaner stage, optical microscopy analysis is performed to determine the relative density of the samples using ImageJ [53] software. ImageJ converts microscopy images into grayscale, followed by automated thresholding applied to the cross-sectional images of the samples to quantify their relative density. Subsequently, the polished surfaces are swabbed with a cotton stick soaked in Kalling's Reagent to etch the samples and reveal their microstructural details. Kalling's Reagent facilitates the visualisation of melt pool boundaries and sub-grain microstructures, which are examined using both optical microscopy and SEM. Following etching, EDS analysis was performed on 10 different regions, including cellular boundaries and interior areas, to assess the elemental composition. The lineal intercept method, defined as the ratio of the total length of lines by the number of intercepts (see Equation (1)), is used to measure the average cellular size structure in DPM-processed SS316L.

$$\bar{l} = \frac{L}{N_I} \qquad \text{Eq. 1}$$

Here L denotes the total length of test lines, N_I is the number of intercepts, and $\bar{l}$ represents the average cell size.

Before etching, the sample with the highest relative density is analysed using XRD to identify crystallographic phases. This is followed by an in-depth microstructural investigation through EBSD using a JEOL-7900F Schottky Field Emission Scanning Electron Microscope. Additionally, nanoindentation is conducted at 9 different points in a 3 × 3 array using an open-loop trapezoidal loading and unloading approach with the Micro Materials NanoTest Vantage system, applying a load of 20 mN. Subsequently, the Vickers hardness of all samples was measured using a Zwick Roell Indentec ZHV30 Vickers hardness tester, applying a 0.5 kgf load. Six separate hardness measurements are performed on the polished cross-sections of each sample to minimise the influence of random variations during testing.

Most studies in the literature on processing SS316L using LPBF utilise the Volumetric Energy Density (VED) formulation to optimise process parameters [54,55] and understand the mechanical properties of the fabricated parts [56], although its limitations have been highlighted in several studies [57,58]. Thomas et al. [59] proposed a new formulation called Normalised Energy Density (NED), which incorporates not only process parameters such as laser power, scanning speed, layer thickness, and hatch distance, but also material-specific properties, including laser absorptivity, specific heat capacity, density, and melting temperature, which are factors not considered in the conventional VED formulation. Therefore, NED formulation has been shown to offer a more comprehensive explanation of process behavior compared to VED. NED is defined as the ratio of q^* (dimensionless beam power) to the product of l^* (dimensionless layer thickness), v^* (dimensionless scanning speed) and h^* (dimensionless hatch distance), as shown in Equation (2). This formulation incorporates both processing parameters and material properties within a unified, dimensionless framework.

$$E_0^* = \frac{q^*}{v^* l^* h^*} = \frac{Aq}{2vlh}\,\frac{1}{\rho C_p (T_m - T_0)} \qquad \text{Eq. 2}$$

Where A is the laser absorptivity of powder, ρ is the density (kg/m^3) of the powder, q is a laser power (W), l is a layer thickness (m), h is the hatch distance (m), v is scanning speed (m/s), C_p is the specific heat (J/kg.K) of the powder, T_m is the melting temperature (K) of the powder and T_0 is the initial temperature (K) of the system.

3. Results

3.1. Porosity and energy density analysis

Fig. 3 illustrates the relative density distribution of DPM-processed SS316L samples with two hatch distance values, 75 µm and 100 µm, corresponding to 50 % and 33 % laser beam overlap, across varying scanning speeds ranging from 750 to 1800 mm/min (12.5–30 mm/s, see Table 2). Additionally, optical microscopy images are presented above the relative density distribution to highlight regions of high, medium, and low porosity in the sample processed with a scanning speed of 1500 mm/min and a hatch distance of 100 µm.

A notable difference in porosity is observed among the samples fabricated with varying hatch distances. Specifically, samples produced with a hatch distance of 100 µm exhibit higher density across all scanning speeds compared to those with a 75 µm hatch distance. Hatch distance plays a critical role in determining melt pool overlap; excessive overlap can induce random flow patterns within the molten track, which in turn promotes pore formation in the final parts [60]. Porosity in the samples increases with scanning speeds up to 1500 mm/min (25 mm/s), beyond which a decline in relative density is observed, as illustrated in Fig. 3. A similar trend, where relative density initially increases and then decreases with increasing scanning speed, has been reported in the literature for SS316L processed via LPBF. [21]. This behaviour can be attributed to the high energy input at low scanning speeds, which can lead to keyhole formation in the melt pool because of intense metal vaporisation. The maximum relative density of 98.1 % is achieved in the sample processed with a scanning speed of 1500 mm/min and a hatch distance of 100 µm. However, some regions within this sample exhibit densities exceeding 99 %, as shown in Fig. 3.

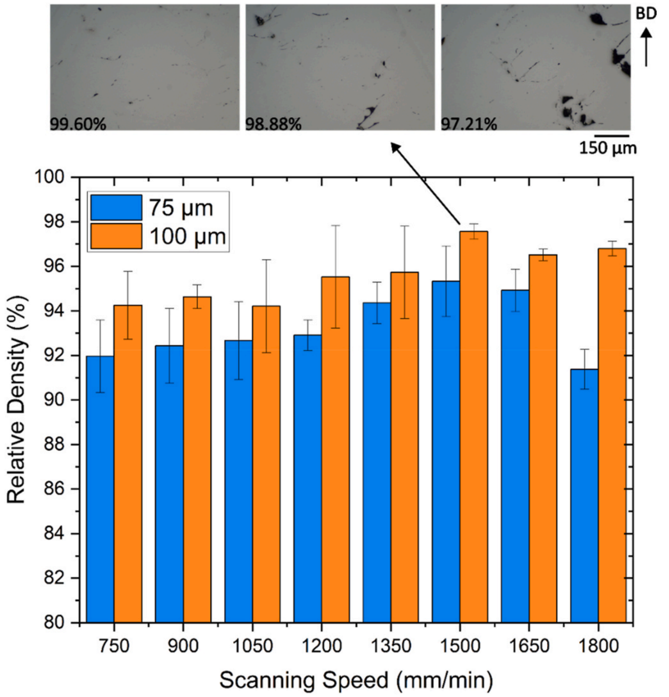

Fig. 3. Relative density of all samples varying scanning speeds (from 750 to 1800 mm/min) and hatch distances (75 and 100 µm) with porosity maps.

Table 2
The relative density and NED values for all samples.

Laser Power (W)	Scanning Speed (mm/min)	Hatch Distance (µm)	Relative Density (%)	NED
35	750	75	91.97 ± 1.63	90.56
	900		92.43 ± 1.68	75.47
	1050		92.67 ± 1.75	64.69
	1200		92.91 ± 0.68	56.60
	1350		94.36 ± 0.93	50.31
	1500		95.33 ± 1.59	45.28
	1650		95.02 ± 0.95	41.16
	1800		91.38 ± 0.9	37.73
	750	100	94.25 ± 2.96	67.92
	900		94.63 ± 0.53	56.60
	1050		94.11 ± 2.09	48.51
	1200		95.52 ± 2.3	42.45
	1350		95.72 ± 2.07	37.73
	1500		**97.77 ± 0.35**	**33.96**
	1650		96.52 ± 0.26	30.87
	1800		96.8+±0.33	28.30

The relative density and NED values of all samples, along with their corresponding processing parameters, are presented in Table 2. The sample with the highest relative density is highlighted. Table 2 demonstrates that NED serves as a useful indicator of relative density in the fabricated samples. Samples with high NED values (greater than 45) generally exhibit poor relative density (<95 %), likely due to excessive energy input causing vaporisation and over-melting. Conversely, samples with lower NED values (below 45) tend to achieve higher relative density (>95 %) in general. These results suggest that while NED provides a valuable metric for predicting densification outcomes, individual process parameters such as hatch distance and scanning speed also play significant roles and must be optimised independently.

Fig. 4 presents a comparison of literature data for SS316L processing via LPBF (having >99 % relative density) alongside the best-performing DPM sample in terms of relative density, plotted against the NED diagram. In our previous work, the higher energy requirement for processing SS316L with diode lasers, in comparison to Ti6Al4V, was thoroughly examined using NED mapping [61].

SS316L has a higher density and thermal conductivity compared to Ti6Al4V [45], making it more challenging to process using a low-energy slow moving laser spot (the laser spot size is 100 μm by 150 μm, see Fig. 2). It is therefore recommended to use a more powerful diode laser to increase the scanning speed and overcome the challenges posed by the high thermal conductivity of SS316L, to achieve near-full density (∼99.9 %) comparable to LPBF results reported in the literature.

From this point onward, all independent analyses, including optical microscopy, SEM, XRD, EBSD, and nanoindentation, except for Vickers hardness, are performed on the sample exhibiting the highest relative density. This corresponds to the specimen processed at a scanning speed of 1500 mm/min with a hatch distance of 100 μm.

3.2. *Microstructural characterisation*

After etching with Kalling's Reagent, the melt pool boundaries become visible in the optical microscopy images, as shown in Fig. 5(a). The hierarchical microstructure, resulting from the layer-by-layer fabrication using DPM, is presented in both the optical microscopy image (Fig. 5(a)) and the SEM images (Fig. 5(b)–(e)). When a new layer is deposited onto the previously melted layer, the laser partially remelts the underlying layer, resulting in overlapping, as indicated by the yellow dotted ellipse in Fig. 5(a). Additionally, the dotted white squares in Fig. 5(a) highlight the overlapping of crescent-shaped melt pools, which occurs due to the hatch distance employed during scanning. Detailed microstructural images captured using SEM are presented in Fig. 5(b), with melt pool boundaries distinctly highlighted by dotted white arcs.

Fig. 5(c) clearly illustrates the growth of columnar grains along the building direction through the melt pool boundaries. In this process, the previously solidified layer serves as a seed for the recently melted layer during rapid solidification [49]. Epitaxial growth of columnar grains follows the direction of heat flow, which aligns with the building direction and is perpendicular to the melt pool curvature [49,66]. Fig. 5(d) illustrates the primary sub-grain microstructure, which consists of cellular dendrites. Both columnar and cellular structures arise from the solidification process associated with laser processing in DPM.

The size of the cellular structure in LPBF-processed SS316L has been reported in previous studies as < 1 μm [8], 275.2 ± 24.6 nm [67], 330–590 nm [68], and 400–850 nm [69]. According to solidification theory, the ratio of the high thermal gradient (G) to the crystal growth rate (R) has an impact on cellular dendrite formation. Additionally, the cooling rate during solidification is determined by the product of G and R [40]. An increase in crystal growth rate, driven by a higher scanning speed, given the correlation between the solidification rate (R) and scanning speed [20] leads to an overall increase in the cooling rate of the process. For instance, in LPBF-processed SS316L, an increase in cellular size from 250 to 1200 nm has been observed as the scanning speed decreases from 7000 mm/s to 283 mm/s [19]. Recently, Erman et al. [61] investigated the cellular structure size of SS316L processed using Diode Area Melting (DAM) with 450 nm blue diode lasers, reporting a range of 3–4 μm, highlighting the inherently slower cooling rate of the process. Fig. 5(e) explicitly highlights the region encompassed by the cellular sub-grain structure. The cellular structure is calculated by the lineal intercept method by 1.97 μm in DPM-processed SS316L (see Fig. 5 (e)). The cooling rate in the DPM process can be estimated using an empirical relationship based on the dendritic spacing of SS316L. This relationship is generally expressed as [70]:

$$d = 80\dot{T}^{-0.33} \qquad \text{Eq. 3}$$

where $\dot{T}$ (K/s) is the cooling rate, and d is the dendritic spacing. Based on the formula, the cooling rate of the DPM process is estimated to be 6.66×10^4 K/s. The cooling rate of SS316L processing in DPM falls between that of LPBF and DAM techniques (ranging from 10^7 to 600 $\frac{°C}{s}$ [71]). Consequently, the resulting cellular structure size lies between those observed in these two processes.

Fig. 6(a) shows the inverse pole figure (IPF) from the plane, which is parallel to the building direction (cross-section plane against scanning direction, shown as a dotted square in Fig. 6(a)). Fig. 6 reveals the presence of columnar grains, which are attributed to the high thermal gradient along the building direction during solidification. Grain growth is observed to extend across the melt pool boundaries along the build direction, spanning approximately 3–4-layer thicknesses, as shown in Fig. 6(a). Additionally, the grain width remains consistently smaller than the laser spot size (see Fig. 6(a), spot size is 150 μm in width), indicating the absence of significant lateral growth.

The grain size of parts produced by laser processing technologies depends on the cooling rate and increases as the cooling rate decreases [72]. The presence of larger grain sizes under slower cooling conditions arises from the extended time available for grain growth [73]. Additionally, the grain size may vary within the sample along the building direction due to high thermal conduction between the substrate and the sample. A finer microstructure is expected in the region of the sample close to the substrate; therefore, EBSD measurements are conducted from the middle of the sample. The average grain size in DPM-processed SS316L is measured to be 17.6 μm in the region shown in Fig. 6(a), which is approximately five times larger than that of fine-grained LPBF counterparts (3.2–3.4 μm) [74] and about twice as large as typical LPBF grain sizes (7.6 μm) [15]. Although some studies have reported higher grain sizes in typical LPBF samples, ranging from 12.6 to 16.7 μm [49, 52,75]. The grain size observed in DPM-processed SS316L still exceeds these values when measured on a cross-section parallel to the building direction (i.e., perpendicular to the scanning direction).

EBSD analysis indicates the absence of a strong crystallographic texture, suggesting no preferential grain orientation across the analysed region. A relatively weak alignment of the <101> and <111> crystallographic directions is observed in the BD-TD plane. The weak texture intensity is further supported by the {100}, {110}, and {111} pole figures shown in Fig. 6(b), with a maximum intensity value reaching 8.53.

Furthermore, the influence of crystallographic orientation on Young's modulus was evaluated using the texture information obtained through EBSD, applying the Hill approximation. The Hill approximation, which represents the arithmetic mean of the Reuss (lower bound)

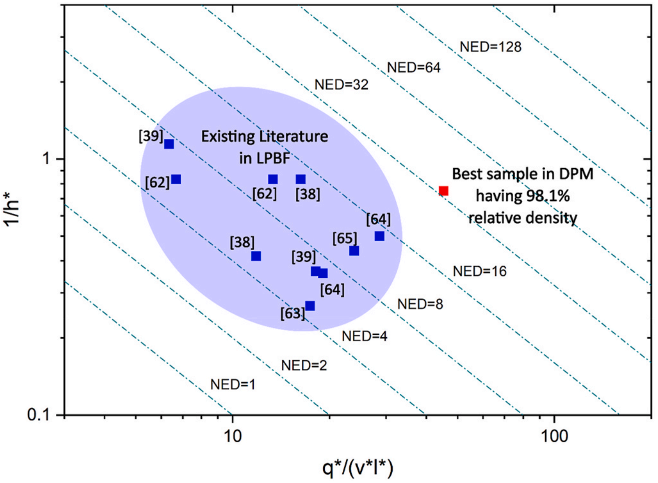

Fig. 4. NED diagram for the best sample in DPM in terms of porosity and literature works [38,39,62–65] for processing SS316L in LPBF.

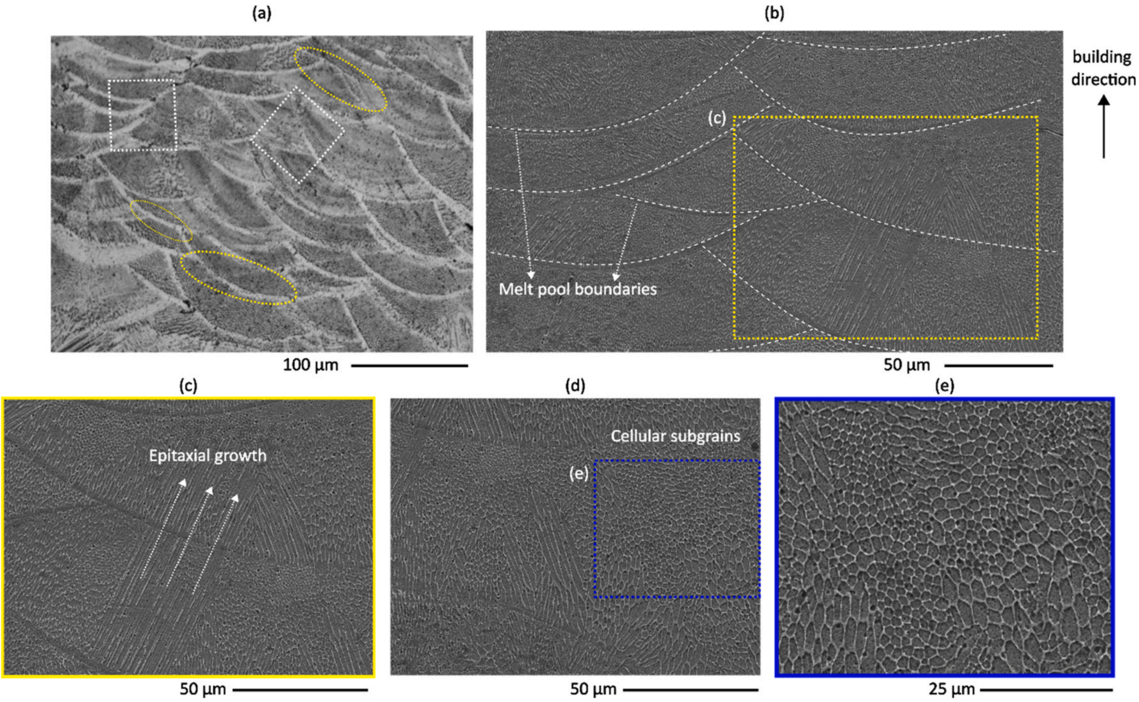

Fig. 5. (A) Optical microscopy image representing melt pool boundaries at 20× magnification., (b) SEM image showing melt pool boundaries at 1kx, (c) SEM image highlighting epitaxial growth of columnar structures at 2kx magnification., (d) SEM image showing cellular structures at 2kx magnification., (e) close-up view of cellular structures under SEM at 4kx magnification.

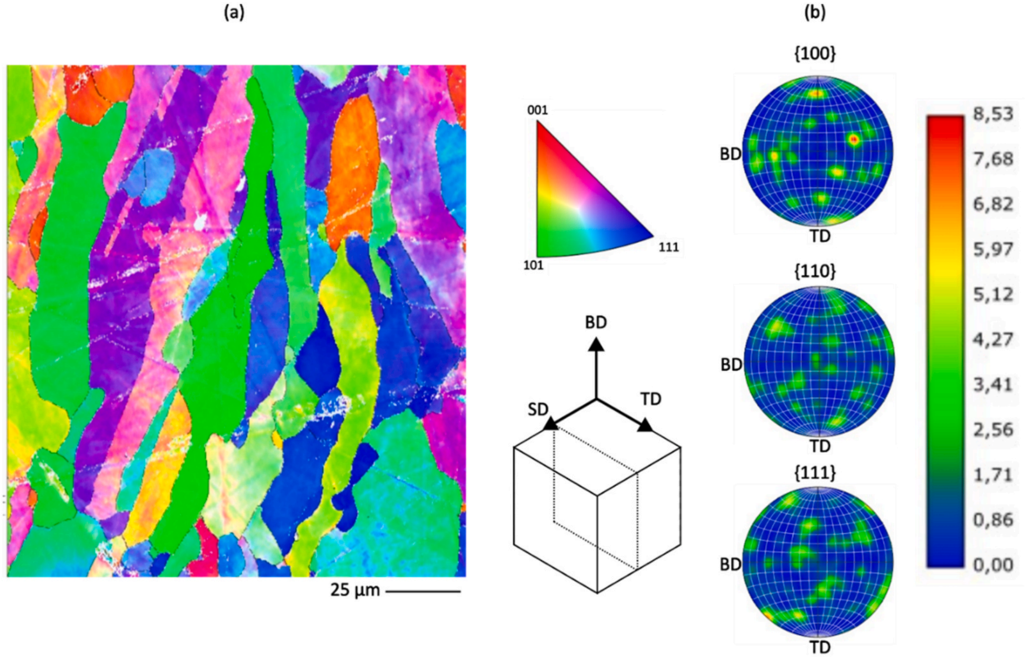

Fig. 6. (A) EBSD inverse-pole figure (IPF) map, (b) pole figures for {100}, {110}, and {111} crystallographic planes.

and Voigt (upper bound) models, is employed to estimate the macroscopic elastic properties of LPBF-processed samples [76,77]. The elastic modulus values calculated using the Hill approximation along different directions, $E_{BD} = 190.96\ GPa, E_{TD} = 175.09\ GPa,$ indicate the absence of significant crystallographic texture in the DPM-processed SS316L, as evidenced by the relatively small difference (~10 %) between the two directions. Moreover, these calculated values are consistent with the experimentally measured elastic modulus values, which will be presented in the nanoindentation test section.

Grain interference is classified as low-angle grain boundaries (LAGBs) when the misorientation is less than 10° and high-angle grain boundaries (HAGBs) when it exceeds 10°. The presence of LAGBs, along with the formation of cellular structures and high dislocation densities, has been attributed to the enhanced ductility and strength of LPBF-processed SS316L [8]. According to EBSD analysis, the fraction of LAGBs in DPM-processed SS316L is 71.2 %, and HAGBs constitute 28.8 %. The high proportion of LAGBs is attributed to the extensive cellular structure network within the microstructure, which contributes to strengthening by impeding dislocation motion [15]. The low fraction of HAGBs is also attributed to the reduced residual stress resulting from rapid solidification [24].

3.3. Phase determination and elemental composition analysis

XRD analysis is conducted for phase identification on both the virgin powder and the DPM-processed sample with the highest relative density. The analysis is performed in the region where the normal vector of the plane is oriented perpendicular to the building direction, as illustrated in Fig. 7(a). The XRD diffraction peaks in Fig. 7(a) indicate the presence of (111), (200), (220), (311), and (222) crystallographic planes. XRD results confirm the presence of the γ-austenite phase exclusively, which is consistent with literature data on SS316L processing in LPBF [52,63,78]. It is noteworthy that no other intermetallic compounds, such as δ-ferrite corresponding to the (110) crystallographic plane, were observed following the (111) austenite peak. The formation of the δ-ferrite phase is suppressed by the high cooling rates in LPBF [37], a phenomenon that also applies to the DPM process. As outlined in Section 3.2, SS316L samples processed via DAM, with inherently slower cooling rates than those in DPM and LPBF, show the presence of the δ-ferrite phase [61]. It is also observed that the austenite peaks in the DPM-processed sample are broader compared to the powder material. This broadening can be attributed to the residual stress and dislocation density induced by the thermal cycling and rapid solidification inherent in laser processing [55].

Fig. 7(b) and (c) present the EDS mapping at the sub-grain level, revealing the cellular structure along with the corresponding elemental composition, respectively. Fig. 7(b) indicates that the boundaries of the cellular structures are enriched with chromium (Cr) and manganese (Mn). Elements such as Cr, molybdenum (Mo), and silicon (Si) are known α-phase stabilisers and are typically observed in regions containing ferrite [40]. It is important to note that Cr (shown in red in Fig. 7(b)) is observed at the cellular boundaries, consistent with the literature; however, the accumulation of Si or Mo at the boundaries is not evident [40]. However, EBSD and XRD analyses did not detect the presence of ferrite phases in the DPM-processed SS316L samples, which is consistent with the absence of significant accumulation of α-stabilizing elements.

3.4. Micro-hardness measurements

Fig. 8 presents the Vickers hardness values of DPM-processed SS316L samples with 75 μm and 100 μm hatch distances at varying scanning speeds. Additionally, hardness data from the literature for cast and wrought SS316L are included for comparison in Fig. 8(a) and (b), respectively. The Vickers hardness values of the samples range from 204.3 H V to 229.3 H V, with an average hardness of 215.3 H V. The average micro-hardness of LPBF-processed SS316L samples ranges from 216 H V to 235 H V [10,39,74,79,80] that are presented in Fig. 8(a) and (b), with some extreme values reaching up to 315 H V [81] reported in the literature. Cherry et al. [79] emphasised that the decrease in Vickers hardness is primarily attributed to increased porosity. However, no clear correlation between hardness and relative density is observed in DPM-processed samples. Therefore, the discrepancy in hardness results between DPM and LPBF samples may be attributed to the slightly higher proportion of porosity in DPM samples, as well as the inherently slower cooling rate. Even though the hardness values of some DPM-processed samples are close to those of LPBF-processed samples, the average hardness of DPM samples is 10–20 H V lower compared to LPBF-processed SS316L. Yet, it is noticeably higher than traditionally processed SS316L, such as cast and wrought samples, as shown in Fig. 8 (a) and (b).

Sun et al. [39] suggested that the variation in hardness values among LPBF samples can be attributed to differences in the size of the cellular structure at the sub-grain level, which result from changes in the induced cooling rate. The etched cross-sections (Fig. 5(e)) clearly show that the cellular structure size in DPM samples is larger than in LPBF-processed samples. Previously, the hardness of DAM-processed SS316L samples, which exhibited a larger cellular structure compared to DPM samples, was reported to be approximately 180 H V [61]. Moreover, EBSD measurements reveal that the grain size in DPM-processed samples is 5 times larger than that observed in LPBF samples. This inverse relationship between grain size and hardness aligns with the Hall–Petch relation, which predicts a decrease in

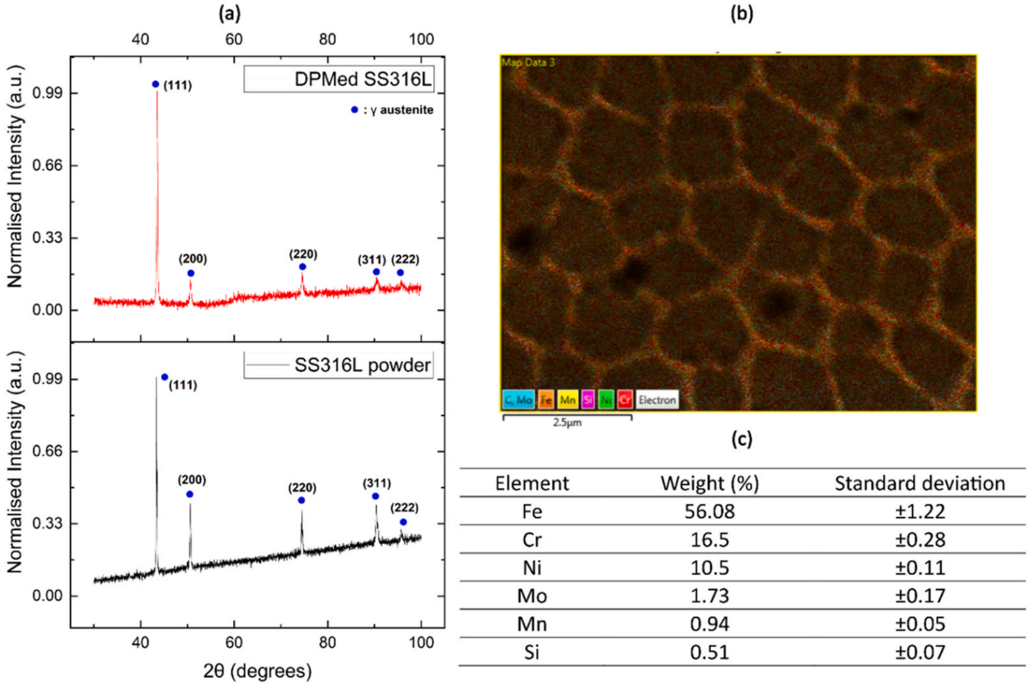

Element	Weight (%)	Standard deviation
Fe	56.08	±1.22
Cr	16.5	±0.28
Ni	10.5	±0.11
Mo	1.73	±0.17
Mn	0.94	±0.05
Si	0.51	±0.07

Fig. 7. (A) XRD pattern of the DPM-processed SS316L and the virgin SS316L powder, (b) EDS maps for elemental segregation over cellular structure, (c) chemical composition of the area presented in Fig. 7(b).

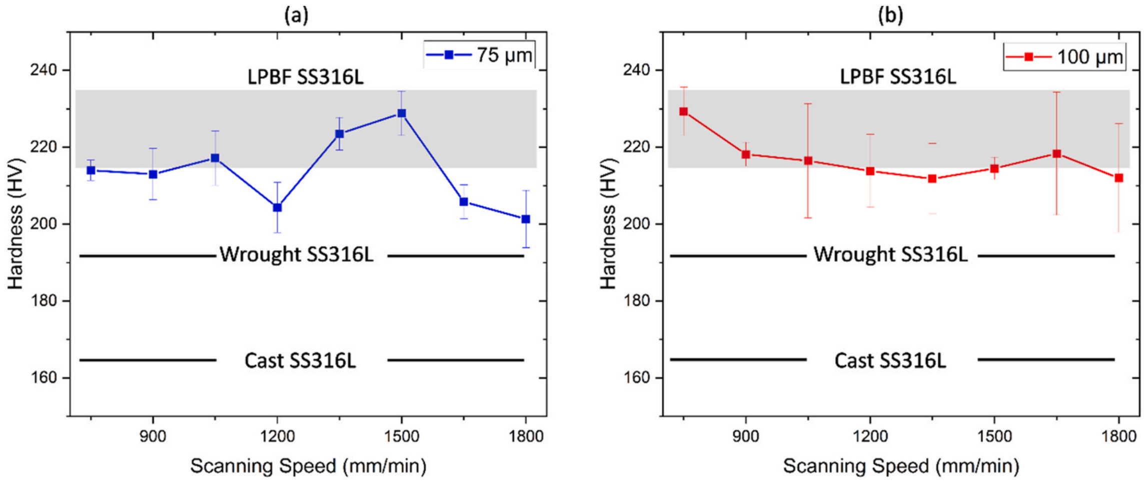

Fig. 8. Vickers hardness of DPM-processed SS316L samples (a) having a 75 μm hatch distance, (b) having a 100 μm hatch distance with cast SS316L [52], wrought SS316L [80], and LPBF SS316L [10,39,74,79,80].

hardness with increasing grain size. Additionally, the fluctuations observed in the micro-hardness data of DPM-processed SS316L can be attributed to the specific regions where indentations were performed. Measurements taken at grain boundaries typically yield higher hardness values compared to those taken within the grain interiors. Furthermore, data collected from regions with finer grains tend to show higher hardness values compared to areas with larger grain structures [82]. Additionally, the hardness of SS316L samples produced via LPBF increases with increasing relative density [83]. Therefore, the lower hardness observed in DPM samples compared to LPBF counterparts may be attributed to their lower relative density.

3.5. Nano-indentation test

Fig. 9 presents the typical load-displacement curve obtained from nanoindentation tests. Based on nine nanoindentation points, the maximum nano-hardness value is measured as 5.03 GPa, while the minimum is 3.68 GPa. These values are comparable to those observed in LPBF-processed parts, which exhibit a maximum nano-hardness of up to 6 GPa, particularly within grains exhibiting well-defined cellular substructures [66]. Furthermore, the fluctuations observed in Fig. 9 during the loading and unloading phases of the nanoindentation test can be attributed to the presence of defects such as balling and porosity, as well as the resistance offered by the cellular substructure [66]. The variation in nano-hardness values in DPM-processed SS316L can be attributed to the specific indentation locations, particularly whether they intersect cellular boundaries, as well as differences in the size of the cellular structures. Guo et al. [40] reported that the nano-hardness of EBM-processed SS316L was 3.25 ± 0.15 GPa at cellular boundaries, whereas it was 2.88 ± 0.11 GPa within the cellular interiors. Kong et al. demonstrated that LPBF-fabricated parts with finer cellular structures exhibited higher nano-hardness values compared to those with larger cellular structures [19].

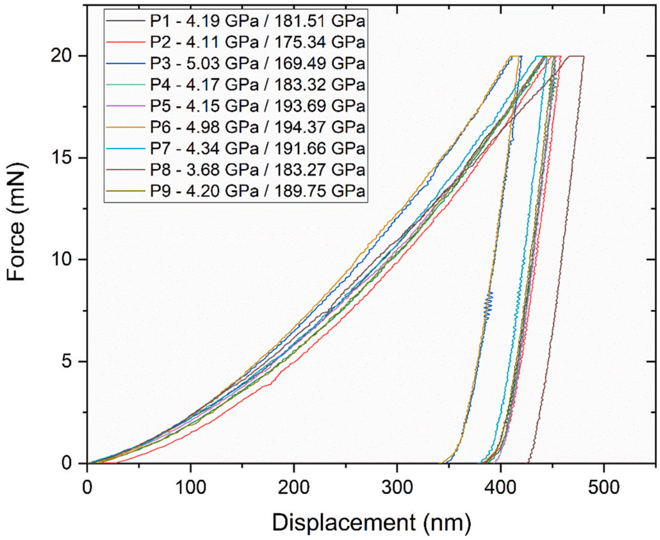

Fig. 9. Load-displacement curve of DPM-processed SS316L obtained from nano-indentation test with nano-hardness and elastic modulus results.

Another contributing factor to the variation in nano hardness measurements in DPM is micro-level anisotropy, which arises from the layer-wise nature of the manufacturing process and directional solidification of the melt pool [84]. Furthermore, variations in nano hardness measurements can result from differences in the crystallographic orientation of the grains where the data are collected [18].

In addition to the nano-hardness values of DPM-processed SS316L, the reduced modulus measured via nanoindentation ranged from 169.49 GPa to 194.37 GPa (see Fig. 9). These values are comparable to those reported for LPBF-processed SS316L [18,85,86], except for some works [66,74] that shows higher values due to fine microstructure. The slight reduction in the elastic modulus of DPM-processed SS316L compared to LPBF counterparts, like the trend observed in Vickers hardness values, can be attributed to grain coarsening, as evidenced by the EBSD results.

4. Discussion

4.1. Remelting

Fig. 10 presents the optical microscopy images of samples subjected to 50 % and 100 % power remelting. There is no significant increase in relative density observed in the remelted samples compared to the as-built DPM samples; the relative density of the remelted specimens remains within the range presented in Fig. 3. In conclusion, the highest relative density obtained in this study is 98.1 %, corresponding to a scanning speed of 1500 mm/min and a hatch distance of 100 μm. Porosity observed in the remelted samples is highlighted with dotted white circles and rectangles in Fig. 10(a) and (b). The melt pool boundaries are indicated by double yellow and green arrows in Fig. 10 (a) and (b), respectively. The melt pool boundaries in the remelted samples are noticeably shallower compared to those in the as-built DPM samples, indicating a reduced penetration depth during remelting (see

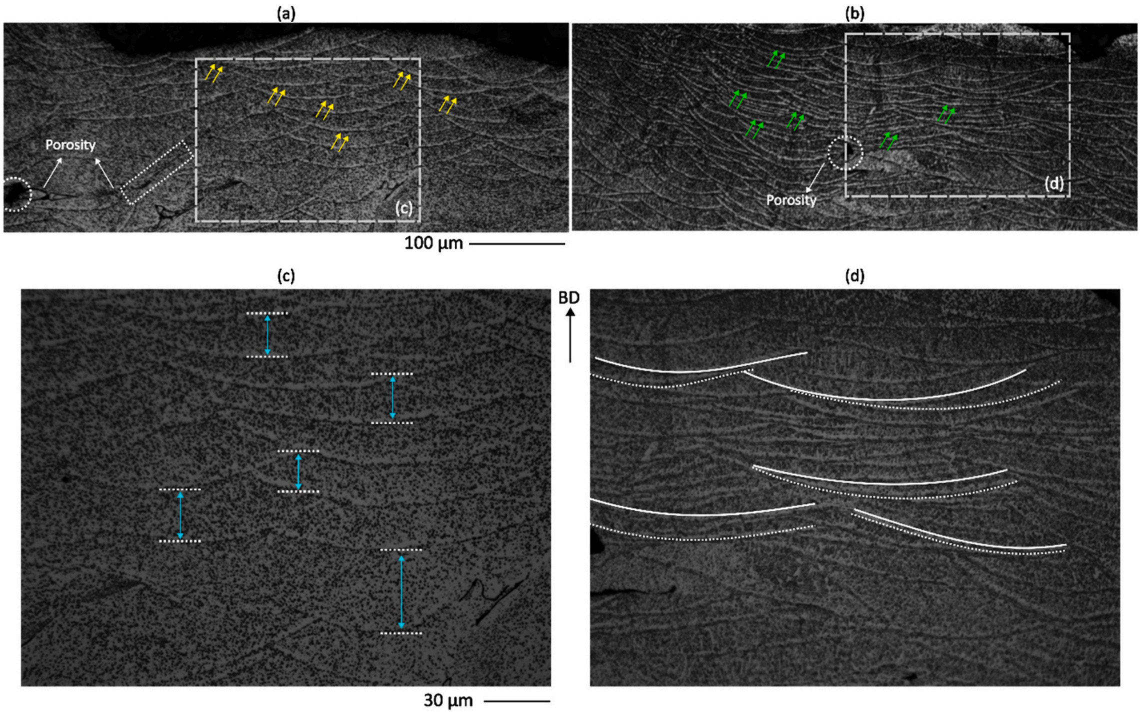

Fig. 10. Optical microscopy image representing melt pool boundaries at 20× magnification for (a) 50 % remelting, (b) 100 % remelting, close-up view of melt pool boundaries at 50× magnification for (c) 50 % remelting, (d) 100 % remelting.

Fig. 5(a)). Yasa et al. [87] also demonstrated that, following remelting, the melt pool geometry transitions from the typically curved shape observed in conventionally LPBF-produced SS316L to a more linear form. The double-headed arrows indicate the melt pool depth in the sample remelted at 50 % power in Fig. 10(c). Although the melt depth is shallower than that of the as-built DPM sample (see Fig. 5(a)), it is greater than that observed in the sample remelted at 100 % power (see Fig. 10(d)).

Higher-magnification micrographs in Fig. 10(c) and (d), corresponding to the regions outlined by dotted grey rectangles in Fig. 10(a) and (b), offer a more detailed view of melt pool formation. Furthermore, a distinct secondary melting boundary is visible in the sample remelted at 100 % power, indicating deeper thermal penetration during the second pass. This feature is highlighted in Fig. 10(d) using solid and dotted white arcs to represent the first and second melting boundaries, respectively. This phenomenon has also been observed during the processing of SS316L using LPBF with dual lasers, where one laser functions as the primary forming laser and the other serves as a control laser [26].

4.2. The effect of cooling rate on microstructure

Fig. 11 shows the variation of cellular structure size with scanning speed in the same sample along the build direction. The sample is produced using the optimal scanning speed parameters based on the densification results. The schematics in the top right corner of Fig. 11 illustrate the cross-section of the sample. The cellular structure observed at the bottom part of the sample exhibits distinct characteristics compared to the middle and top regions, primarily due to the rapid solidification that occurs between the first deposited layer and the relatively cold substrate [22]. To mitigate this effect, a support structure is included in the sample; however, this region was not subjected to further analysis.

The average cellular structure sizes were measured as 1.39 µm, 1.27 µm, 1.17 µm, and 1.10 µm for the regions processed at scanning speeds of 1200 mm/min, 1350 mm/min, 1500 mm/min, and 1800 mm/min, respectively. The decreasing trend in cellular structure size with increasing scanning speed, along with the standard deviation calculated from 10 measurements for each parameter, is shown in Fig. 11. A notable point is that the decreasing trend in cellular structure size remains evident even when higher scanning speeds are applied in the upper layers. This highlights the dominant influence of process-parameter selection, particularly scanning speed. Even though the reduced heat transfer to the substrate in the upper layers [73], the cooling rate decreases, emphasising the dominant role of scanning-speed selection. The direct correlation between scanning speed and the cooling rate during SS316L processing has been previously validated in LPBF studies [19]. A decreasing trend in cellular structure size with increasing scanning speed was observed, where scanning speeds of 7000 mm/s,

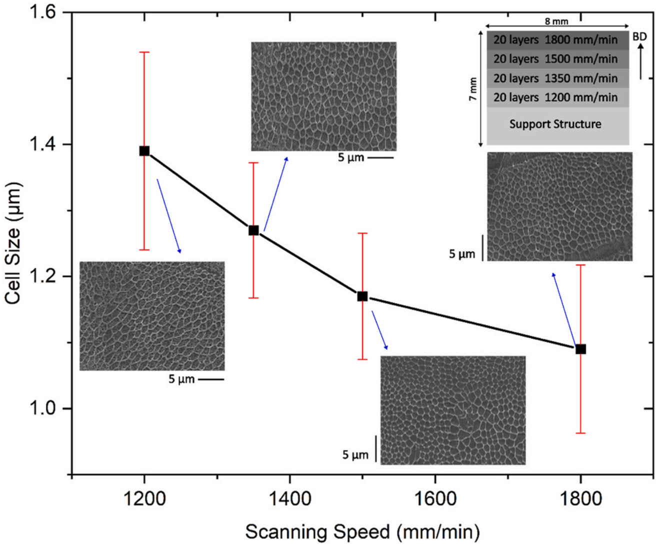

Fig. 11. The size of cellular structures in the sample produced with varying scanning speeds.

4250 mm/s, 850 mm/s, and 283 mm/s corresponded to average cell sizes of approximately 200 nm, 250 nm, 500 nm, and 1 μm, respectively [88].

Several studies have been conducted to create bimetallic structures using different powders to combine their advantages — for example, producing bimetallic samples with IN718 and SS316L to leverage their superior properties in high-stress, high-corrosion, and high-temperature environments [89]. The cellular structure also plays a significant role in determining the strength and ductility of the material. This approach is considered a promising avenue for understanding and controlling the microstructure of SS316L samples, particularly in terms of cellular structure size. Mechanical testing is needed for future implementation to more thoroughly evaluate the effectiveness of this approach.

4.3. Overall comparison of results in DPM vs LPBF

Table 3 provides an overall comparison of the two processing technologies, LPBF and DPM, in terms of grain size, cellular structure size, cooling rate, microhardness, nano-hardness, and elastic modulus. It is demonstrated that SS316L (having >98 % relative density) parts exhibit average microhardness and nano-hardness values of approximately 215 H V and 4.32 GPa, respectively, comparable to those of LPBF-fabricated counterparts. The slower cooling rate in DPM processing leads to grain coarsening (~18 μm) and a noticeable increase in sub-grain cellular structures in SS316L (to ~2 μm), compared to parts produced via LPBF (~6.66 × 10^4 K/s vs 10^7 K/s). Further investigation into the cellular structure size reveals that it increases as the scanning speed decreases, which is attributed to the corresponding reduction in the cooling rate. It is important to highlight that no significant reduction in micro- and nano-hardness is observed despite the grain coarsening in DPM-processed SS316L. Elastic modulus measurements, both experimental and theoretical, reveal that DPM-processed SS316L exhibits an average value of approximately 185 GPa, which is comparable to that of LPBF-produced counterparts. Remelting of the sample affects the melt pool shape, transforming it from a curved to a more linear geometry. Further increase in remelting power results in the formation of secondary melt boundaries adjacent to the previously solidified layers.

Table 3
Overall comparison of LPBF and DPM processes.

	LPBF	DPM
Grain Size (μm)	3.2–16.8 [15,49,52,69,74,75]	17.6
Cell Size (μm)	0.275-0.85 [8,67–69]	1.97
NED	3.6–14.3 [38,39,62–65]	33.96
Cooling rate (K/s)	10^5-10^8 [90,91]	~6.66x10^4
Micro-hardness (HV)	216-235 [10,39,74,79,80]	204.3–229.3
Nano-hardness (GPa)	1.92-6.0 [49,66,74,84,86]	3.68–5.03
Elastic Modulus (GPa)	162.5–230 [18,66,86]	169.49–194.37

5. Conclusion

This work has explored the processing of SS316L using Diode Point Melting (DPM), a low-cost short-wavelength blue diode laser technique characterised by lower cooling rates compared to conventional LPBF. The inherently slower solidification in DPM offers a unique thermal control during fabrication, but the higher thermal conductivity and density of SS316L, relative to Ti6Al4V, introduce processing challenges.

Through optimisation of process parameters, relative densities of up to 98.1 % were achieved at a scanning speed of 1500 mm/min and hatch spacing of 100 μm. These conditions required substantially higher normalised energy density (NED) values than those typical for LPBF, with the best-performing samples reaching 33.96 compared to the LPBF range of 3.6–14.3. The resulting microstructures are markedly coarser than LPBF counterparts, with average grain sizes of 17.6 μm and cellular structures of 1.97 μm, in contrast to the 3.2–16.8 μm grains and 0.275–0.85 μm cells commonly reported for LPBF-fabricated SS316L. This coarsening, together with the higher porosity inherent to the current DPM process, contributed to the observed reductions in both micro- and nano-hardness.

Analysis of multi-speed builds revealed a clear relationship between scanning speed and microstructural refinement. Decreasing the scanning speed increased the cellular structure size from 1.1 ± 0.13 μm to 1.39 ± 0.15 μm. This capability to influence microstructure through build orientation and layer-specific parameter adjustment highlights the potential of DPM for application-specific tailoring of mechanical properties.

Overall, this study establishes a first benchmark for processing SS316L via DPM, confirming both the viability and the current limitations of this approach. While coarser microstructures and higher porosity presently limit mechanical performance, the demonstrated thermal control, parameter sensitivity, and low-cost system architecture suggest that with improved energy delivery and porosity reduction strategies, DPM could evolve into a competitive alternative to LPBF for cost-sensitive 3D printing of metallic components.

To summarise the outcomes of this research.

- DPM enables the fabrication of high-density additively manufactured parts (>98 %) while providing improved thermal control using diode lasers.
- A grain size of 17.6 μm and a cell size of 1.97 μm were observed in DPM-processed SS316L, attributable to the lower estimated cooling rate (≈6.66 × 10^4 K s^{-1}) compared with conventional LPBF (~10^7 K s^{-1}).
- Mechanical properties comparable to LPBF were achieved, including a Vickers hardness of 215.3 H V, nano-hardness values of 3.68–5.03 GPa, and a reduced modulus of 169.49–194.37 GPa.
- Remelting produced a shallower melt pool relative to as-built DPM samples.
- Layer-wise adjustment of process parameters (e.g., scanning speed) enabled microstructural tailoring along the build direction, particularly with respect to cellular structure size.

Author contribution

Sefer Can Erman: Writing - original draft, Formal analysis, Investigation, Methodology, Visualisation. Alkim Aydin: Formal analysis, Methodology, Visualisation, Writing – review & editing. Kamran Mumtaz: Conceptualisation, Supervision, Writing – review & editing

Declaration of competing interest

The authors declare the following financial interests/personal relationships which may be considered as potential competing interests. Kamran Mumtaz reports financial support was provided by Engineering and Physical Sciences Research Council. Sefer Can Erman reports financial support was provided by Turkish Government Ministry of Education. If there are other authors, they declare that they have no known competing financial interests or personal relationships that could have appeared to influence the work reported in this paper.

Acknowledgement

This study is supported by the Turkish Government Ministry of Education and the UK Research and Innovation, Engineering and Physical Sciences Research Council (EPSRC Grant EP/W024764/1). The authors gratefully acknowledge Dr Erhan Cetin's assistance with the methodology.

Data availability

The data that support the findings of this study are available from the corresponding author, S. Can Erman, upon reasonable request.

References

[1] Haghdadi N, Laleh M, Moyle M, Primig S. Additive manufacturing of steels: a review of achievements and challenges. J Mater Sci 2021;56(1):64–107. https://doi.org/10.1007/s10853-020-05109-0.

[2] Keller C, Tabalaiev K, Marnier G, Noudem J, Sauvage X, Hug E. Influence of spark plasma sintering conditions on the sintering and functional properties of an ultra-fine grained 316L stainless steel obtained from ball-milled powder. Mater Sci Eng A 2016;665:125–34. https://doi.org/10.1016/j.msea.2016.04.039.

[3] Song R, Xiang J, Hou D. Characteristics of mechanical properties and microstructure for 316L austenitic stainless steel. J Iron Steel Res Int 2011;18(11):53–9. https://doi.org/10.1016/S1006-706X(11)60117-9.

[4] Kong D, Ni X, Dong C, Lei X, Zhang L, Man C, Yao J, Cheng X, Li X. Bio-functional and anti-corrosive 3D printing 316L stainless steel fabricated by selective laser melting. Mater Des 2018;152:88–101. https://doi.org/10.1016/j.matdes.2018.04.058.

[5] Mohammadi Zahrani E, Saatchi A, Alfantazi A. Pitting of 316L stainless steel in flare piping of a petrochemical plant. Eng Fail Anal 2010;17(4):810–7. https://doi.org/10.1016/j.engfailanal.2009.10.015.

[6] Sedriks AJ. Corrosion resistance of austenitic fe-cr-ni-mo alloys in marine environments. Int Met Rev 1982;27(1):321–53. https://doi.org/10.1179/imr.1982.27.1.321.

[7] Hryniewicz T, Rokosz K, Filippi M. Biomaterial studies on AISI 316L stainless steel after magnetoelectropolishing. Materials 2009;2(1):129–45. https://doi.org/10.3390/ma2010129.

[8] Wang YM, Voisin T, McKeown JT, Ye J, Calta NP, Li Z, Zeng Z, Zhang Y, Chen W, Roehling TT, Ott RT, Santala MK, Depond PJ, Matthews MJ, Hamza AV, Zhu T. Additively manufactured hierarchical stainless steels with high strength and ductility. Nat Mater 2018;17(1):63–71. https://doi.org/10.1038/nmat5021.

[9] Alsalla HH, Smith C, Hao L. Effect of build orientation on the surface quality, microstructure and mechanical properties of selective laser melting 316L stainless steel. Rapid Prototyp J 2018;24(1):9–17. https://doi.org/10.1108/RPJ-04-2016-0068.

[10] Tolosa I, Garciandía F, Zubiri F, Zapirain F, Esnaola A. Study of mechanical properties of AISI 316 stainless steel processed by 'selective laser melting', following different manufacturing strategies. Int J Adv Manuf Technol 2010;51(5–8):639–47. https://doi.org/10.1007/s00170-010-2631-5.

[11] Shunmugavel M, Polishetty A, Goldberg M, Singh R, Littlefair G. A comparative Study of mechanical properties and machinability of Wrought and additive manufactured (Selective laser melting) titanium alloy – Ti-6Al-4V. Rapid Prototyp J 2017;23(6):1051–6. https://doi.org/10.1108/RPJ-08-2015-0105.

[12] Challis VJ, Xu X, Halfpenny A, Cramer AD, Saunders M, Roberts AP, Sercombe TB. Understanding the effect of microstructural texture on the anisotropic elastic properties of selective laser melted Ti-24Nb-4Zr-8Sn. Acta Mater 2023;254:119021. https://doi.org/10.1016/j.actamat.2023.119021.

[13] Riemer A, Leuders S, Thöne M, Richard HA, Tröster T, Niendorf T. On the fatigue crack growth behavior in 316L stainless steel manufactured by selective laser melting. Eng Fract Mech 2014;120:15–25. https://doi.org/10.1016/j.engfracmech.2014.03.008.

[14] Sun Z, Tan X, Tor SB, Chua CK. Simultaneously enhanced strength and ductility for 3D-Printed stainless steel 316L by selective laser melting. NPG Asia Mater 2018;10(4):127–36. https://doi.org/10.1038/s41427-018-0018-5.

[15] Chepkoech M, Owolabi G, Warner G. Investigation of microstructures and tensile properties of 316L stainless steel fabricated via laser powder bed fusion. Materials 2024;17(4):913. https://doi.org/10.3390/ma17040913.

[16] Fergani O, Brotan V, Bambach M, Pérez-Prado MT. Texture evolution in stainless steel processed by selective laser melting and annealing. Mater Sci Technol 2018;34(18):2223–30. https://doi.org/10.1080/02670836.2018.1523518.

[17] Sohrabpoor H, Salarvand V, Lupoi R, Chu Q, Li W, Aldwell B, Stanley W, O'Halloran S, Raghavendra R, Choi CH, Brabazon D. Microstructural and mechanical evaluation of post-processed SS 316L manufactured by laser-based powder bed fusion. J Mater Res Technol 2021;12:210–20. https://doi.org/10.1016/j.jmrt.2021.02.090.

[18] Uddin MJ, Ramirez-Cedillo E, Mirshams RA, Siller HR. Nanoindentation and Electron Backscatter diffraction mapping in laser powder bed fusion of stainless steel 316L. Mater Char 2021;174:111047. https://doi.org/10.1016/j.matchar.2021.111047.

[19] Kong D, Dong C, Ni X, Zhang L, Li X. Cellular size dependence on the strength of additively manufactured austenitic stainless steel. Mater Lett 2020;279:128524. https://doi.org/10.1016/j.matlet.2020.128524.

[20] Bertoli US. Stability of cellular microstructure in laser powder bed fusion of 316L stainless steel. 2019.

[21] Hao L, Wang W, Zeng J, Song M, Chang S, Zhu C. Effect of scanning speed and laser power on formability, microstructure, and quality of 316L stainless steel prepared by selective laser melting. J Mater Res Technol 2023;25:3189–99. https://doi.org/10.1016/j.jmrt.2023.06.144.

[22] Barode J, Brander M, Yu T, Nadimpalli VK, Jensen DJ, Wang X. Cell structure in LPBF 316L—Microstructural heterogeneity, thermal stability, and mechanical properties. Materials 2025;18(3):475. https://doi.org/10.3390/ma18030475.

[23] Krakhmalev P, Fredriksson G, Svensson K, Yadroitsev I, Yadroitsava I, Thuvander M, Peng R. Microstructure, solidification texture, and thermal stability of 316 L stainless steel manufactured by laser powder bed fusion. Metals 2018;8(8):643. https://doi.org/10.3390/met8080643.

[24] Li W, Meng L, Niu X, Zhou W. Microstructure, mechanical properties, and deformation behaviour of LPBF 316L via post-heat treatment. Virtual Phys Prototyp 2024;19(1):e2405623. https://doi.org/10.1080/17452759.2024.2405623.

[25] Gao S, Li Z, Van Petegem S, Ge J, Goel S, Vas JV, Luzin V, Hu Z, Seet HL, Sanchez DF, Van Swygenhoven H, Gao H, Seita M. Additive manufacturing of alloys with programmable microstructure and properties. Nat Commun 2023;14(1):6752. https://doi.org/10.1038/s41467-023-42326-y.

[26] Liu Z, Yang Y, Xiao Y, Lei H, Yang C, Liu Z, Zhao Q, Song C. Investigation of 316L microstructure evolution mechanism and mechanical properties in dual-laser powder bed fusion with controllable remelting time interval. Mater Des 2024;239:112761. https://doi.org/10.1016/j.matdes.2024.112761.

[27] Navarre C, Cayron C, Buttard M, Jamili AM, Logé RE. Tailoring mechanical properties and microstructures in laser powder bed fusion of 316 L stainless steel through aluminium alloying and combined Ex-Situ and in-Situ heat treatments. Addit Manuf 2025;97:104620. https://doi.org/10.1016/j.addma.2024.104620.

[28] Elkaseer A, Charles A, Schneider S, Scholz SG. Part tailoring in metal-additive manufacturing: a step towards functionally graded customized stainless-steel components using laser powder bed fusion. Appl Sci 2022;12(12):6193. https://doi.org/10.3390/app12126193.

[29] Sofinowski KA, Raman S, Wang X, Gaskey B, Seita M. Layer-wise engineering of grain orientation (LEGO) in laser powder bed fusion of stainless steel 316L. Addit Manuf 2021;38:101809. https://doi.org/10.1016/j.addma.2020.101809.

[30] Harrison NJ, Todd I, Mumtaz K. Reduction of micro-cracking in nickel superalloys processed by selective laser melting: a fundamental alloy design approach. Acta Mater 2015;94:59–68. https://doi.org/10.1016/j.actamat.2015.04.035.

[31] Buchbinder D, Meiners W, Pirch N, Wissenbach K, Schrage J. Investigation on reducing distortion by preheating during manufacture of aluminum components using selective laser melting. J Laser Appl 2014;26(1):012004. https://doi.org/10.2351/1.4828755.

[32] Bartlett JL, Li X. An overview of residual stresses in metal powder bed fusion. Addit Manuf 2019;27:131–49. https://doi.org/10.1016/j.addma.2019.02.020.

[33] Liu Y, Hu Z, Wang L, Zhai Z, Yan W, Li Z. A new mechanism for laser absorption in high-reflectivity metal powder beds modified with ceramic particles. J Appl Phys 2025;137(13):133101. https://doi.org/10.1063/5.0252992.

[34] Ye C, Zhang C, Zhao J, Dong Y. Effects of post-processing on the surface finish, porosity, residual stresses, and fatigue performance of additive manufactured metals: a review. J Mater Eng Perform 2021;30(9):6407–25. https://doi.org/10.1007/s11665-021-06021-7.

[35] Gao B, Zhao H, Peng L, Sun Z. A review of research progress in Selective Laser Melting (SLM). Micromachines 2022;14(1):57. https://doi.org/10.3390/mi14010057.

[36] Gargalis L, Ye J, Strantza M, Rubenchik A, Murray JW, Clare AT, Ashcroft IA, Hague R, Matthews MJ. Determining processing behaviour of pure Cu in laser powder bed fusion using direct micro-calorimetry. J Mater Process Technol 2021;294:117130. https://doi.org/10.1016/j.jmatprotec.2021.117130.

[37] Tucho WM, Lysne VH, Austbø H, Sjolyst-Kverneland A, Hansen V. Investigation of effects of process parameters on microstructure and hardness of SLM manufactured SS316L. J Alloys Compd 2018;740:910–25. https://doi.org/10.1016/j.jallcom.2018.01.098.

[38] Leicht A, Rashidi M, Klement U, Hryha E. Effect of process parameters on the microstructure, tensile strength and productivity of 316L parts produced by laser powder bed fusion. Mater Char 2020;159. https://doi.org/10.1016/j.matchar.2019.110016.

[39] Sun Z, Tan X, Tor SB, Yeong WY. Selective Laser melting of stainless steel 316L with low porosity and high build rates. Mater Des 2016;104:197–204. https://doi.org/10.1016/j.matdes.2016.05.035.

[40] Guo S, Xu J, Gu J, Peng Y, Zhou Q, Wang K. Effect of cellular structure on the mechanical properties of 316L stainless steel fabricated by EBF3. J Mater Res Technol 2023;25:5469–82. https://doi.org/10.1016/j.jmrt.2023.07.024.

[41] Huang G, Wei K, Deng J, Liu M, Zeng X. High-Power Laser powder bed fusion of 316L stainless steel: defects, microstructure, and mechanical properties. J Manuf Process 2022;83:235–45. https://doi.org/10.1016/j.jmapro.2022.08.066.

[42] Zhao X, Wang T. "Laser Powder Bed Fusion of Powder Material: a Review," 3D print. Addit Manuf 2023;10(6):1439–54. https://doi.org/10.1089/3dp.2021.0297.

[43] Wei LC, Ehrlich LE, Powell-Palm MJ, Montgomery C, Beuth J, Malen JA. Thermal conductivity of metal powders for powder bed additive manufacturing. Addit Manuf 2018;21:201–8. https://doi.org/10.1016/j.addma.2018.02.002.

[44] Brandau B, Da Silva A, Wilsnack C, Brueckner F, Kaplan AFH. Absorbance Study of powder conditions for laser additive manufacturing. Mater Des 2022;216. https://doi.org/10.1016/j.matdes.2022.110591.

[45] Aydin A, Cetin E, Erman SC, Mumtaz K. Laser powder bed fusion of Ti6Al4V using low-cost high efficiency 450 Nm diode point melting. J Mater Res Technol 2025;34:2814–27. https://doi.org/10.1016/j.jmrt.2024.12.252.

[46] Aydin A, Cetin E, Mumtaz K. In-Situ dynamic Laser Area heating during diode point melting for thermal gradient reduction in laser powder bed fusion. Mater Des 2025;260:114985. https://doi.org/10.1016/j.matdes.2025.114985.

[47] Curiel FF, García R, López VH, González-Sánchez J. Effect of magnetic field applied during gas metal arc welding on the resistance to localised corrosion of the heat affected Zone in AISI 304 stainless steel. Corros Sci 2011;53(7):2393–9. https://doi.org/10.1016/j.corsci.2011.03.022.

[48] Zavala-Arredondo M, Boone N, Willmott J, Childs DTD, Ivanov P, Groom KM, Mumtaz K. Laser diode area melting for high speed additive manufacturing of metallic components. Mater Des 2017;117:305–15. https://doi.org/10.1016/j.matdes.2016.12.095.

[49] Zhai W, Zhou W, Zhu Z, Nai SML. Selective Laser melting of 304L and 316L stainless steels: a comparative Study of microstructures and mechanical properties. Steel Res Int 2022;93(7):2100664. https://doi.org/10.1002/srin.202100664.

[50] Im Y-D, Kim K-H, Jung K-H, Lee Y-K, Song K-H. Anisotropic mechanical behavior of additive manufactured AISI 316L steel. Metall Mater Trans A 2019;50(4):2014–21. https://doi.org/10.1007/s11661-019-05139-7.

[51] Barrionuevo GO, La Fé-Perdomo I, Ramos-Grez JA, Walczak M, Mendez PF. Microstructural differences and mechanical performance of stainless steel 316L conventionally processed versus a selective laser melted. Prog Addit Manuf 2024. https://doi.org/10.1007/s40964-024-00774-y.

[52] Bartolomeu F, Buciumeanu M, Pinto E, Alves N, Carvalho O, Silva FS, Miranda G. 316L stainless steel mechanical and tribological Behavior—A comparison between selective laser melting, hot pressing and conventional casting. Addit Manuf 2017; 16:81–9. https://doi.org/10.1016/j.addma.2017.05.007.

[53] Schneider CA, Rasband WS, Eliceiri KW. NIH image to ImageJ: 25 years of image analysis. Nat Methods 2012;9(7):671–5. https://doi.org/10.1038/nmeth.2089.

[54] Diaz Vallejo N, Lucas C, Ayers N, Graydon K, Hyer H, Sohn Y. Process optimization and microstructure analysis to understand laser powder bed fusion of 316L stainless steel. Metals 2021;11(5):832. https://doi.org/10.3390/met11050832.

[55] Choi J-P, Shin G-H, Brochu M, Kim Y-J, Yang S-S, Kim K-T, Yang D-Y, Lee C-W, Yu J-H. Densification behavior of 316L stainless steel parts fabricated by selective laser melting by variation in laser energy density. Mater Trans 2016;57(11): 1952–9. https://doi.org/10.2320/matertrans.M2016284.

[56] Douglas R, Beard W, Barnard N, Lee S, Shao S, Shamsaei N, Jones T, Lancaster R. The influence of energy density on the low cycle fatigue behaviour of laser powder bed fused stainless steel 316L. Int J Fatigue 2024;181:108123. https://doi.org/10.1016/j.ijfatigue.2023.108123.

[57] Scipioni Bertoli U, Wolfer AJ, Matthews MJ, Delplanque JPR, Schoenung JM. On the limitations of volumetric energy density as a design parameter for selective laser melting. Mater Des 2017;113:331–40. https://doi.org/10.1016/j.matdes.2016.10.037.

[58] Smith C, Hommer G, Keeler M, Gockel J, Findley K, Brice C, Clarke A, Klemm-Toole J. Assessing volumetric energy density as a predictor of defects in laser powder bed fusion 316L stainless steel. JOM 2025;77(2):737–48. https://doi.org/10.1007/s11837-024-06946-z.

[59] Thomas M, Baxter GJ, Todd I. Normalised model-based processing diagrams for additive layer manufacture of engineering alloys. Acta Mater 2016;108:26–35. https://doi.org/10.1016/j.actamat.2016.02.025.

[60] Mao Y, Gao Y, Hu J, Shen X, Zhou H. Effect of hatch spacing on the quality of inconel 718 alloy part. Materials 2024;17(2):452. https://doi.org/10.3390/ma17020452.

[61] Erman SC, Aydin A, Groom K, Mumtaz K. Diode Area melting of SS316L using low power 450 Nm lasers. Int J Adv Manuf Technol 2025;136(10):4471–90. https://doi.org/10.1007/s00170-025-15090-0.

[62] Kurzynowski T, Gruber K, Stopyra W, Kuźnicka B, Chlebus E. Correlation between process parameters, microstructure and properties of 316 L stainless steel processed by selective laser melting. Mater Sci Eng A 2018;718:64–73. https://doi.org/10.1016/j.msea.2018.01.103.

[63] Yan J, Zhou Y, Gu R, Zhang X, Quach WM, Yan M. A comprehensive Study of steel powders (316L, H13, P20 and 18Ni300) for their selective laser melting additive manufacturing. Metals 2019;9(1). https://doi.org/10.3390/met9010086.

[64] Liverani E, Toschi S, Ceschini L, Fortunato A. Effect of Selective Laser Melting (SLM) process parameters on microstructure and mechanical properties of 316L austenitic stainless steel. J Mater Process Technol 2017;249:255–63. https://doi.org/10.1016/j.jmatprotec.2017.05.042.

[65] Wang D, Liu Y, Yang Y, Xiao D. Theoretical and experimental Study on surface roughness of 316L stainless steel metal parts obtained through selective laser melting. Rapid Prototyp J 2016;22(4):706–16. https://doi.org/10.1108/RPJ-06-2015-0078.

[66] Jeyaprakash N, Saravana Kumar M, Yang C-H, Cheng Y, Radhika N, Sivasankaran S. Effect of microstructural evolution during melt pool Formation on nano-mechanical properties in LPBF based SS316L parts. J Alloys Compd 2024; 972:172745. https://doi.org/10.1016/j.jallcom.2023.172745.

[67] An D, Xiao Y, Liu X, Zhao H, Li X, Chen J. Formation of two distinct cellular structures in 316L stainless steel fabricated by micro-laser beam powder-bed-fusion. Mater Res Lett 2024;12(1):42–9. https://doi.org/10.1080/21663831.2023.2292076.

[68] Li Z, He B, Guo Q. Strengthening and hardening mechanisms of additively manufactured stainless steels: the role of cell sizes. Scr Mater 2020;177:17–21. https://doi.org/10.1016/j.scriptamat.2019.10.005.

[69] Jaskari M, Ghosh S, Miettunen I, Karjalainen P, Järvenpää A. Tensile properties and deformation of AISI 316L additively manufactured with various energy densities. Materials 2021;14(19):5809. https://doi.org/10.3390/ma14195809.

[70] Katayama S, Matsunawa A. Solidification microstructure of laser welded stainless steels. International Congress on applications of lasers & Electro-Optics. Boston, Massachusetts, USA: Laser Institute of America; 1984. p. 60–7. https://doi.org/10.2351/1.5057623.

[71] Alsaddah M, Khan A, Groom K, Mumtaz K. Diode Area melting of Ti6Al4V using 808 Nm Laser sources and variable multi-beam profiles. Mater Des 2022;215. https://doi.org/10.1016/j.matdes.2022.110518.

[72] Shao J, Yu G, He X, Li S, Chen R, Zhao Y. Grain size evolution under different cooling rate in laser additive manufacturing of superalloy. Opt Laser Technol 2019; 119:105662. https://doi.org/10.1016/j.optlastec.2019.105662.

[73] DebRoy T, Wei HL, Zuback JS, Mukherjee T, Elmer JW, Milewski JO, Beese AM, Wilson-Heid A, De A, Zhang W. Additive manufacturing of metallic components – process, structure and properties. Prog Mater Sci 2018;92:112–224. https://doi.org/10.1016/j.pmatsci.2017.10.001.

[74] Kurdi A, Tabbakh T, Basak AK. Microstructural and nanoindentation investigation on the laser powder bed fusion stainless steel 316L. Materials 2023;16(17):5933. https://doi.org/10.3390/ma16175933.

[75] Godec M, Zaefferer S, Podgornik B, Šinko M, Tchernychova E. Quantitative multiscale correlative microstructure analysis of additive manufacturing of stainless steel 316L processed by selective laser melting. Mater Char 2020;160: 110074. https://doi.org/10.1016/j.matchar.2019.110074.

[76] Charmi A, Falkenberg R, Ávila L, Mohr G, Sommer K, Ulbricht A, Sprengel M, Saliwan Neumann R, Skrotzki B, Evans A. Mechanical anisotropy of additively manufactured stainless steel 316L: an experimental and Numerical Study. Mater Sci Eng A 2021;799:140154. https://doi.org/10.1016/j.msea.2020.140154.

[77] Geiger F, Kunze K, Etter T. Tailoring the texture of IN738LC processed by Selective Laser Melting (SLM) by specific scanning strategies. Mater Sci Eng A 2016;661: 240–6. https://doi.org/10.1016/j.msea.2016.03.036.

[78] Shanmuganathan PK, Purushothaman DB, Ponnusamy M. Effect of high laser energy density on selective laser melted 316L stainless steel: analysis on metallurgical and mechanical properties and comparison with Wrought 316L stainless steel. 3D Print Addit Manuf 2023;10(3):383–92. https://doi.org/10.1089/3dp.2021.0061.

[79] Cherry JA, Davies HM, Mehmood S, Lavery NP, Brown SGR, Sienz J. Investigation into the effect of process parameters on microstructural and physical properties of 316L stainless steel parts by selective laser melting. Int J Adv Manuf Technol 2015; 76(5–8):869–79. https://doi.org/10.1007/s00170-014-6297-2.

[80] Yusuf SM, Chen Y, Boardman R, Yang S, Gao N. Investigation on porosity and microhardness of 316L stainless steel fabricated by selective laser melting. Metals 2017;7(2). https://doi.org/10.3390/met7020064.

[81] Saeidi K, Kvetková L, Lofaj F, Shen Z. Austenitic stainless steel strengthened by the in situ Formation of oxide nanoinclusions. RSC Adv 2015;5(27):20747–50. https://doi.org/10.1039/C4RA16721J.

[82] Qu H, Li J, Zhang F, Bai J. Anisotropic cellular structure and texture microstructure of 316L stainless steel fabricated by selective laser melting via rotation scanning strategy. Mater Des 2022;215:110454. https://doi.org/10.1016/j.matdes.2022.110454.

[83] Greco S, Gutzeit K, Hotz H, Kirsch B, Aurich JC. Selective Laser Melting (SLM) of AISI 316L—Impact of Laser power, layer thickness, and hatch spacing on roughness, density, and microhardness at constant input energy density. Int J Adv Manuf Technol 2020;108(5–6):1551–62. https://doi.org/10.1007/s00170-020-05510-8.

[84] England J, Uddin MJ, Ramirez-Cedillo E, Karunarathne D, Nasrazadani S, Golden TD, Siller HR. Nanoindentation hardness and corrosion studies of additively manufactured 316L stainless steel. J Mater Eng Perform 2022;31(8): 6795–805. https://doi.org/10.1007/s11665-022-06703-w.

[85] Röttger A, Boes J, Theisen W, Thiele M, Esen C, Edelmann A, Hellmann R. Microstructure and mechanical properties of 316L austenitic stainless steel processed by different SLM devices. Int J Adv Manuf Technol 2020;108(3):769–83. https://doi.org/10.1007/s00170-020-05371-1.

[86] Ramirez-Cedillo E, Uddin MJ, Sandoval-Robles JA, Mirshams RA, Ruiz-Huerta L, Rodriguez CA, Siller HR. Process planning of L-PBF of AISI 316L for improving surface quality and relating part integrity with microstructural characteristics. Surf Coat Technol 2020;396:125956. https://doi.org/10.1016/j.surfcoat.2020.125956.

[87] Yasa E, Deckers J, Kruth JP. The investigation of the influence of laser Re-Melting on density, surface quality and microstructure of selective laser melting parts. Rapid Prototyp J 2011;17(5):312–27. https://doi.org/10.1108/13552541111156450.

[88] Liu L, Ding Q, Zhong Y, Zou J, Wu J, Chiu Y-L, Li J, Zhang Z, Yu Q, Shen Z. Dislocation network in additive manufactured steel breaks strength–ductility trade-off. Mater Today 2018;21(4):354–61. https://doi.org/10.1016/j.mattod.2017.11.004.

[89] Singh SP, Aggarwal A, Upadhyay RK, Kumar A. Processing of IN718-SS316L bimetallic-structure using laser powder bed fusion technique. Mater Manuf Process 2021;36(9):1028–39. https://doi.org/10.1080/10426914.2021.1885701.

[90] Barrionuevo GO, Ramos-Grez JA, Walczak M, Sánchez-Sánchez X, Guerra C, Debut A, Haro E. Microstructure simulation and experimental evaluation of the anisotropy of 316 L stainless steel manufactured by laser powder bed fusion. Rapid Prototyp J 2023;29(3):425–36. https://doi.org/10.1108/RPJ-04-2022-0127.

[91] Yang J, Yu H, Yin J, Gao M, Wang Z, Zeng X. Formation and control of martensite in Ti-6Al-4V alloy produced by selective laser melting. Mater Des 2016;108: 308–18. https://doi.org/10.1016/j.matdes.2016.06.117.